7
Rare-Earth (Gd, Nd, and Dy) doped $LiMn_{1.5}Ni_{0.5}O_4$ Cathodes

The current Chapter 7 consists of four sections and eight sub-sections. Section 7.1 describes the introduction about current study and section 7.2 presents the physical characterizations of rare-earth doped $LiMn_{1.5}Ni_{0.5}O_4$ (LMNO) cathode for Li-ion battery application. Section 7.3 expresses the electrochemical characterizations of synthesized cathodes. The section 7.2 and 7.3 are divided further into sub-sections. The section 7.2 is classified in four sub-sections namely: 7.2.1 describes the structural parameters, sub-section 7.2.2 describes the surface morphology and elemental detection, sub-section 7.2.3 presents Raman analysis and sub-section 7.2.4 expresses about the porosity and specific surface area of as synthesized cathode materials. The section 7.3 is also sorted in four sub-sections which include cyclic voltammetry study in sub-section 7.3.1, Galvanostatic charge-discharge performance in sub-section 7.3.2, rate performance and cyclability analysis in sub-section 7.3.3 and electrochemical impedance spectroscopy in sub-section 7.3.4. At the end, the concluding remark is covered in section 7.4.

7.1 INTRODUCTION

The lithium ion based cathode materials, layered structural, $LiCoO_2$ (LCO), spinel structure, $LiMn_2O_4$ (LMO), and olivine structure, $LiFePO_4$ (LFP), are major interest among scientific community since past decades [Goodenough at al, 2010]. The LMO cathode material has peculiar features such as high open circuit potential, high energy density, long cyclability, no memory effect, low capacity fading and less toxicity; over the existing lead acid battery technology [Le et al, 2015]. The increasing global demand in high energy density in energy storage systems had made intense search for alternate high operating potential cathode material. The existing wide studied open circuit potential for $LiCoO_2$, $LiMn_2O_4$, and $LiFePO_4$ are 3.9V, 4.0V and 3.4V respectively [Meyers, 2012]. The power density of cathode materials can be increased by increasing the operating potential or current withdrawn from it. The transition metal, Nickel (Ni), doped spinel cathode, $LiMn_{1.5}Ni_{0.5}O_4$ (LMNO), had shown the increase in operating potential 4.7 V with flat plateau [Ma et al, 2016].

The 5 V based spinel LMNO cathode has potential to offer solution for electric vehicle industry because it has ability to provide high energy and power density compared to 4V spinel cathode such as LMO and its derivatives. However, the degradation in capacity, structural instability, and electrolyte instability with long cyclability are major issue to make commercial viable option [Liu and Manthiram, 2009]. The spinel structure based LMNO cathode showed thecapacity fade resulting from an aggressive side reaction with the electrolyte that occurs at high-voltage operation[Mathiram et al, 2014]. One strategy for compete with this issue is the substitution of nickel and/or manganese and/or oxygen in the cubic spinel structure by low amount of different atoms (cations and anions) that also improve the electronic and ionic conductivity of this spinel structure [Yi et al, 2016]. The different atoms, that have been used so far for doping in LMNO spinel structure, are as Al [Zhong et al, 2011], Co [Jang et al, 2012], Cr [Park et al, 2006], Ga [Shin et al, 2011], Mg[Lafont et al, 2009], Mo [Yi at al, 2014], Nb [Yi at al, 2012;], Rh [Wu et al, 2013, Ru [Wang et al,2011], S [Sun et al, 2006], Sm [Mo et al, 2014], Ti [Li at el, 2013], V [Kim et al, 2014], W [Prabakar et al, 2012] and Zn [Yang et al, 2014]. Typically, the doping of LMNO leads to improved cyclic performance and rate capability of the battery. The structural stability and capacity are improved by rare earth metal doping in LMO cathodes [Ram et al, 2016].

The goal of this work is the synthesis, characterization and battery performance evaluation of LMNO doped with different rare earth elements, neodymium (Nd), gadolinium (Gd) and dysprosium (Dy). The cathode samples have coded as in Table 2.1 of Chapter 2. The code name will be used to address these cathodes.

7.2 PHYSICAL CHARACTERIZATION OF RARE-EARTH DOPED $LiMn_{1.5}Ni_{0.5}O_4$ CATHODES

The as-synthesized rare-earth doped cubic spinel phase LMNO cathode powders have characterized for obtaining physical properties. The physical properties of active materials are assessed by adopting different characterization techniques. These characterizations techniques are exploring in consecutive sub-sections from 7.2.1 to 7.2.4 in phased manner as follows:

(7.2.1) *X-ray diffraction and structural analysis* are delivering information about cubic phase formation and lattice parameters.

(7.2.2) *Surface morphology and elemental analysis* are expressing the powder's surface morphology, geometrical shape and size, the elemental present in the sample matrix.

(7.2.3) *Raman spectra and its analysis* is proving the bonding information about the Mn-O/ Ni-O and RE-O.

(7.2.4) *Porosity and specific surface area study* are presenting the porosity and specific surface area of LMNO and RE doped LMO cathode powders by the Brunauer-Emmett-Teller (BET) method.

7.2.1 X-ray Diffraction and Structural Analysis

The X-ray diffraction patterns of LMNO and rare-earth element (Gd, Nd and Dy) doped $LiMn_{1.48}Gd_{0.02}Ni_{0.5}O_4$ (LMNO-Gd02), $LiMn_{1.46}Gd_{0.04}Ni_{0.5}O_4$ (LMNO-Gd04), $LiMn_{1.46}Nd_{0.04}Ni_{0.5}O_4$ (LMNO-Nd04), and $LiMn_{1.46}Dy_{0.04}Ni_{0.5}O_4$ (LMNO-Dy04) have presented in Figure 7.1. The diffraction outlines are recorded in range of 10° to 80° with scan rate 0.02° per second. All the diffractograms are reproducing the cubic spinel phase peaks (space group Fd-3m) according to JCPDS file No. 35-0782 [Manthiram et al, 2014; Yi et al, 2016]. The low amount of impure phase (<10%) observed in LMNO-Nd04 and LMNO-Dy04 cathode samples. The secondary phase are evaluated and identified by the Rietveld method. These impure phases are in the form of Ni_6MnO_8, NiO, Mn_2O_3 and MnO_2 phase and indicated in the Figure 7.1 by star mark.

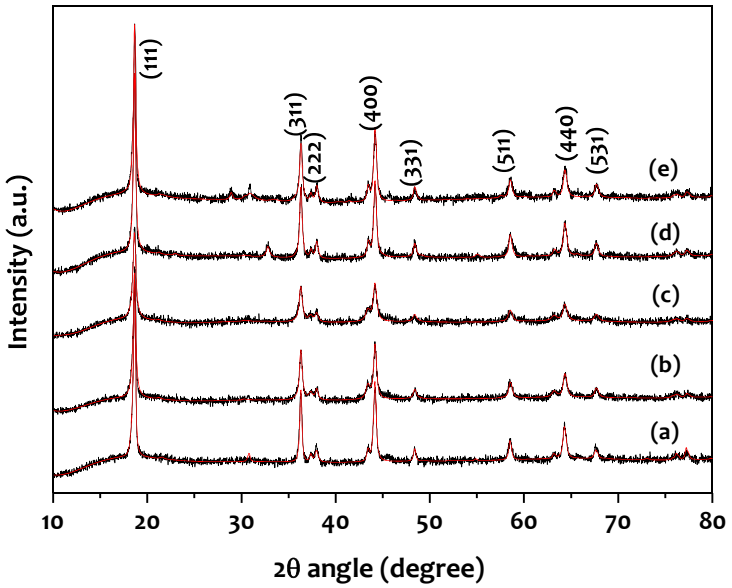

Figure 7.1: Refined (red: calculated; black: experimental) XRD patterns for (a) $LiMn_{1.5}Ni_{0.5}O_4$, (b) $LiMn_{1.48}Gd_{0.02}Ni_{0.5}O_4$, (c) $LiMn_{1.46}Gd_{0.04}Ni_{0.5}O_4$, (d) $LiMn_{1.46}Nd_{0.04}Ni_{0.5}O_4$ and (e) $LiMn_{1.46}Dy_{0.04}Ni_{0.5}O_4$

Table 7.1 presents the lattice parameters, full width at half maxima (FWHM) and the ratio of intensity of plane (311) to plane (400). The lattice constants for $LiMn_{1.50}Ni_{0.5}O_4$, $LiMn_{1.48}Gd_{0.02}Ni_{0.5}O_4$, $LiMn_{1.46}Gd_{0.04}Ni_{0.5}O_4$, $LiMn_{1.46}Nd_{0.04}Ni_{0.5}O_4$ and $LiMn_{1.46}Dy_{0.04}Ni_{0.5}O_4$ are 8.23, 8.24, 8.24, 8.24 and 8.24 Å respectively.

Table 7.1: Lattice Structure Parameters for $LiMn_{1.5}Ni_{0.5}O_4$, $LiMn_{1.48}Gd_{0.02}Ni_{0.5}O_4$ and $LiMn_{1.46}Ni_{0.5}RE_{0.04}O_4$ (RE: Gd, Nd, Dy) powders calcined 800 °C / 14 h

Sample Description	*Lattice Constant*	*Unit cell Volume*	*FWHM*	$I_{(400)}/I_{(311)}$
	(Å)	($Å^3$)	(°)	
LMNO	8.23	556.9	0.29	1.25
LMNO-Gd02	8.24	560.4	0.35	1.14
LMNO-Gd04	8.24	560.4	0.41	1.11
LMNO-Nd04	8.24	558.7	0.28	1.10
LMNO-Dy04	8.24	558.7	0.30	1.28

The lattice constants are observed slightly increase with rare-earth doping with respect to un-doped LMNO cathode. These increase may be attributed to the large ionic radius of rare earth elements Nd^{+3} (0.10 nm) >Gd^{+3} (0.0938 nm) >Dy^{3+} (0.0912 nm) compared to Mn^{3+}(0.064 nm) and Mn^{+4}(0.054 nm). Further, the changes in lattice parameters are an indirect evidence for RE/Mn substitution [Lin et al; 2013].

The value of FWHM for all samples corresponding to the (111) plane peak was analyzed and it is found 0.287° for un-doped $LiMn_{1.50}Ni_{0.5}O_4$ whereas it varies from 0.281° - 0.411° for LMO-Gd02 and $LiMn_{1.5-x}Ni_{0.5}RE_xO_4$ (RE: Gd, Nd, Dy; x=0.04). The absence of impurity phases in LMO-Gd02 and LMO-Gd04 reveals that the Gd^{+3} is able to replace the octahedral site element Mn^{+3}/Mn^{+4} site at 16d. To measure the occupancy of the octahedral site, the peak intensity ratio (400)/(311) was calculated and shown in Table 7.1. The intensity ratio decreases with Gd and Nd elemental doping which supports the octahedral site occupancy whereas in the case of Dy the intensity ratios almost match with un-doped $LiMn_{1.50}Ni_{0.5}O_4$ which indicates the less site occupancy at octahedral site.

7.2.2 Surface Morphology and Elemental Analysis

Figure 7.2 is showing surface morphology of the LMNO powder obtained by SEM and nano-scopic view of surface obtained through HRTEM images of LMNO, LMNO-Gd02, LMNO-Gd04, LMNO-Nd04 and LMNO-Dy04 cathodes powder particles. The SEM image of LMNO, Figure 7.2 (a), is also representative figure for the rest of powder materials. It reveals that powder is in non-homogenous geometry (size and shape) which is confirmed by the HETEM images, Figure 7.2 (b-f). The primary particles average size is in between 200 nm to 50 nm which agglomerated to form large particles. The inset pictures in Figure 7.2 (b-f) are displaying HRTEM images. It should be mentioned here that these images are confirming the crystalline nature of particles. The particle shape is not well defined, but in polyhedron form, in which the smaller polyhedron are assembles together to form large polyhedron secondary particles. Thus, the larger particle sizes are due to agglomeration of small polyhedron grains.

The inset in Figure 7.2 (b) shows that LMNO cathode is not in a well defined planner structure and more faint planar view. Figure 7.2 (c-d), for LMNO-Gd02 and LMNO-Gd04 cathodes, are revealing larger agglomeration trend compared with others spinel cathode powder as evidenced by a faint planar structure. Figure 7.2 (e-f), for LMO-Nd04 and LMO-Dy04 cathode, showed the less agglomerated and finer particle size as compared to the other samples. The inset Figure 7.2 (f) for the powder LMO-Dy04 is demonstrating a well defined structure than the other samples, as confirmed by the clarity and contrast in planar structure.

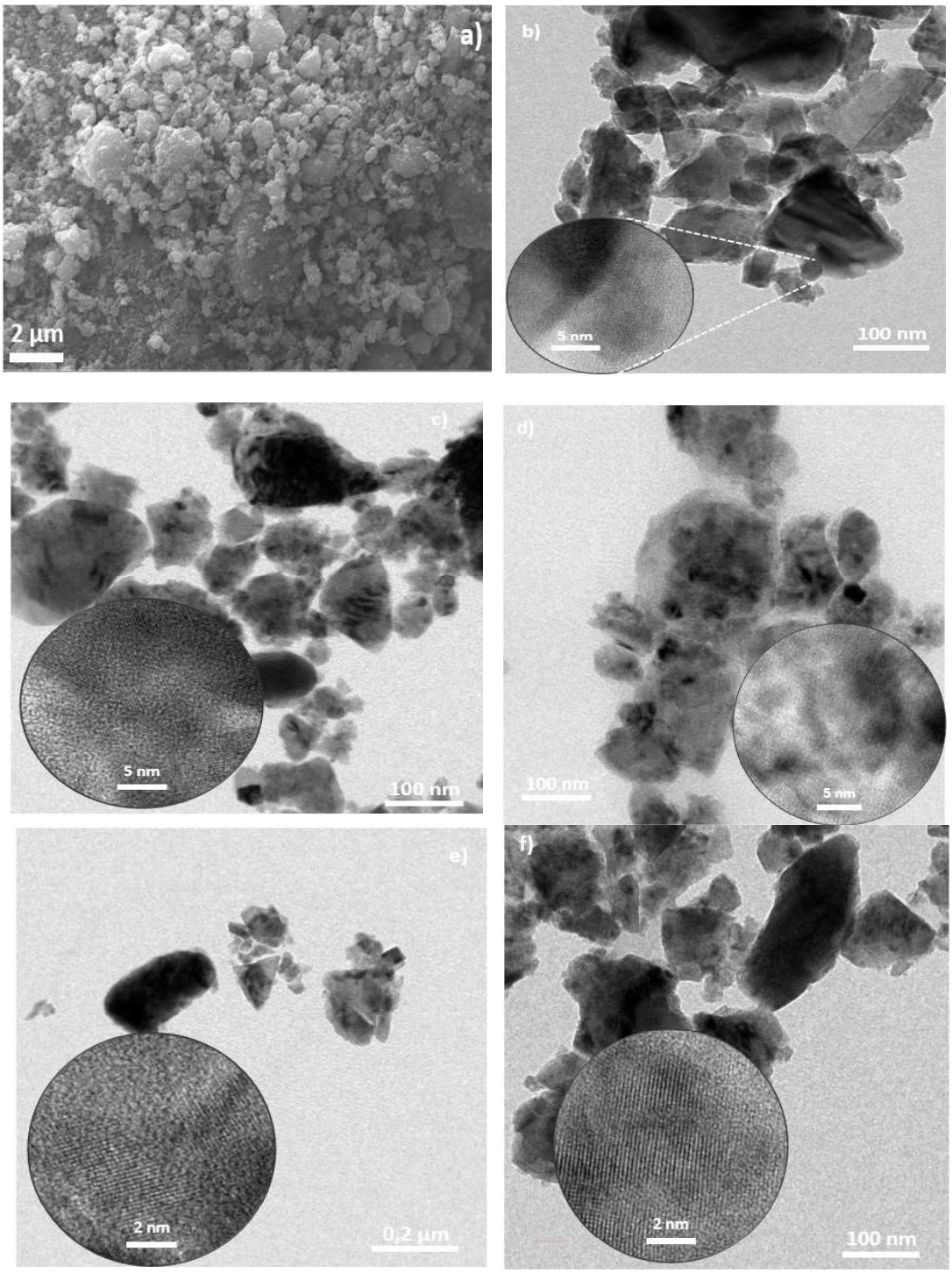

Figure 7.2: (a) SEM image of $LiMn_{1.5}Ni_{0.5}O_4$ and HRTEM images of (b) $LiMn_{1.5}Ni_{0.5}O_4$, (c) $LiMn_{1.48}Ni_{0.5}Gd_{0.02}O_4$, (d) $LiMn_{1.46}Ni_{0.5}Gd_{0.04}O_4$, (e) $LiMn_{1.46}Ni_{0.5}Ny_{0.04}O_4$, and (f) $LiMn_{1.46}Ni_{0.5}Dy_{0.04}O_4$ powders. Inset of HRTEM images shows the atomic arrangement in planner form of the samples

The selected area electron diffraction (SAED) patterns of LMNO and LMNO-Gd02 are recorded and shown in Figure 7.3.

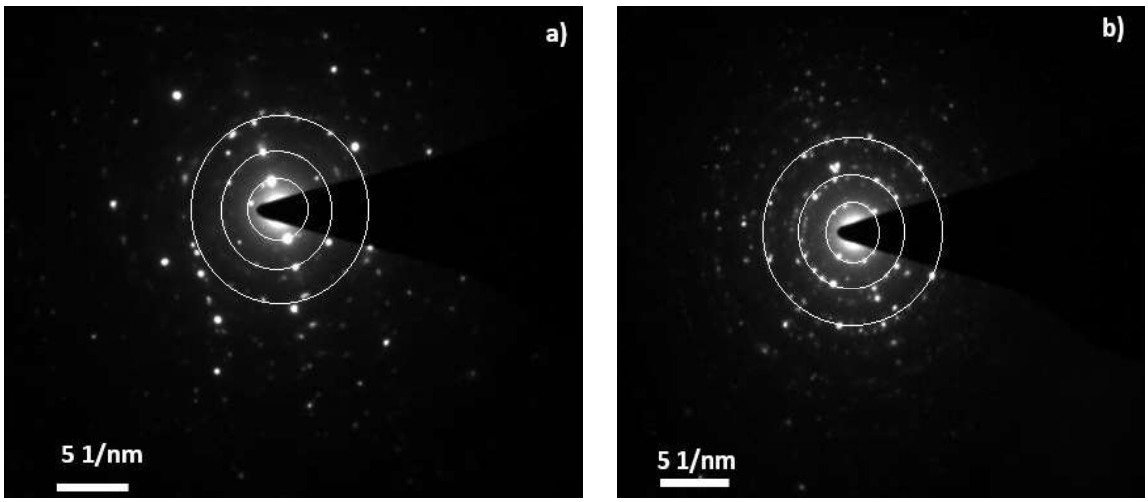

Figure 7.3: SAED patterns for (a) $LiMn_{1.5}Ni_{0.5}O_4$ and (b) $LiMn_{1.48}Ni_{0.5}Gd_{0.02}O_4$ (b) powders

The inner and intense circle corresponds to the (111) plane and the next successive rings correspond to (311) and (400) planes, respectively. After Gd doping, the SAED pattern is more intense and circular which is indicating the tendency for more agglomerated particles formation. Due to this agglomeration, the particle density is increasing which leads to a more intense SAED pattern.

The elemental mapping are analyzed through SEM assisted EDX. The elemental atomic compositions are tabulated in Table 7.2. It is viewed by Table 7.2 that elemental composition of each element (Mn, Ni, O and RE) is expressing slightly deviation from the theoretical values.

Table 7.2: Atomic Composition for$LiMn_{1.5}Ni_{0.5}O_4$, $LiMn_{1.48}Gd_{0.02}Ni_{0.5}O_4$ and $LiMn_{1.46}Ni_{0.5}RE_{0.04}O_4$ (RE: Gd, Nd, Dy) Powders

Sample Description	*Observed Atomic Composition (%)*			
	Mn	*Ni*	*O*	*RE*
LMNO	24.41	7.67	68.92	0.0
LMNO-Gd02	23.85	6.09	69.21	1.05
LMNO-Gd04	23.77	7.65	66.14	2.44
LMNO-Nd04	20.11	7.51	68.15	3.23
LMNO-Dy04	22.98	6.25	68.67	2.10

The elemental mapping results for element (Mn, Ni, O and Dy) are illustrated in Figure 7.4. The Mn, Ni and O elements are detected in the cathode LMNO powder, Figure 7.4 (a-c), whereas the Dy element is detected in cathode LMNO-Dy04 powder as shown in Figure 7.4 (d). The Dy doped sample is treated as reference sample for all doped cathodes.

The Figure 7.4 is expressing uniform distribution of Mn, Ni and O through-out nano-regime. The lower intensity in the case of Dy element is being due to the lower atomic concentration. The mapping of rare-earth element, Dy, doping is also showing homogeneous Dy distribution in the region of samples. The similar results are observed for the rest of elements (Gd, Nd) in their respective cathode matrices.

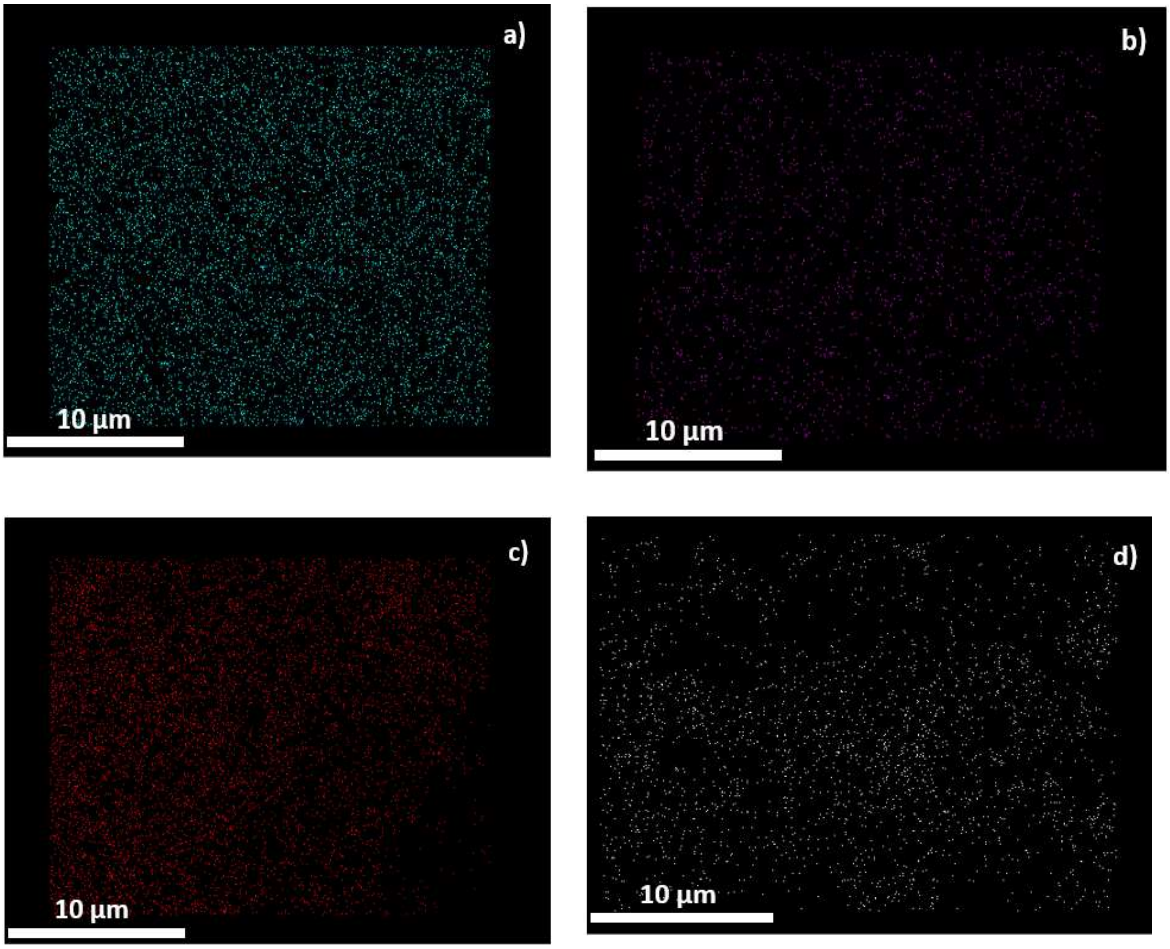

Figure 7.4: EDX mapping for $LiMn_{1.46}Dy_{0.04}Ni_{0.5}O_4$ powder: (a) Mn element, (b) Ni element and (c) O element and (d) Dy element

7.2.3 Raman Spectrum and its Analysis

The Raman spectra were recorded for pristine spinel LMNO and doped LMNO-Gd02, LMNO-RE04 (RE: GD, Nd, Dy) cathode samples and results are shown in Figure 7.5. The two major vibration peaks are observed at 625 cm^{-1} and 488 cm^{-1} in all cathode materials as tabulated in table 7.3. These peaks are characteristics for the Fd3m phase [Julien and Massot, 2003].

Table 7.3: Raman Vibrational Peaks and BET Parameters of $LiMn_{1.5}Ni_{0.5}O_4$, $LiMn_{1.48}Gd_{0.02}Ni_{0.5}O_4$ and $LiMn_{1.46}Ni_{0.5}RE_{0.04}O_4$ (RE: Gd, Nd, Dy) Powders

Sample Description	*Raman Vibrational Peaks*		*BET Parameters*	
	Li-O	Mn-O	Surface area	Average pore size
	(cm^{-1})	(cm^{-1})	(m^2/g)	(nm)
LMNO	488	625	15	3.1
LMNO-Gd02	488	631	12	3.0
LMNO-Gd04	488	628	21	3.2
LMNO-Nd04	488	630	15	3.2
LMNO-Dy04	488	630	15	3.0

The intense peak at 625 cm^{-1} followed by a weak shoulder around 580 cm^{-1} are assigned to the symmetric stretching (A_{1g}), and symmetric bending (F^1_{2g}) vibration modes of Mn-O-Mn/Ni/RE of the MnO_6 group, respectively. However, a weak shoulder corresponding to an asymmetric stretching vibration mode is appearing at 641 cm^{-1}. The symmetric stretching mode

of Li-O vibration in the LiO_4 tetrahedron site is becoming visible at 488 cm^{-1}. The symmetric stretching vibration frequency in Mn-O shifts towards lower wave numbers which may be ascribed to the replacement of $Mn^{3+/4+}$ with more massive RE-ion.

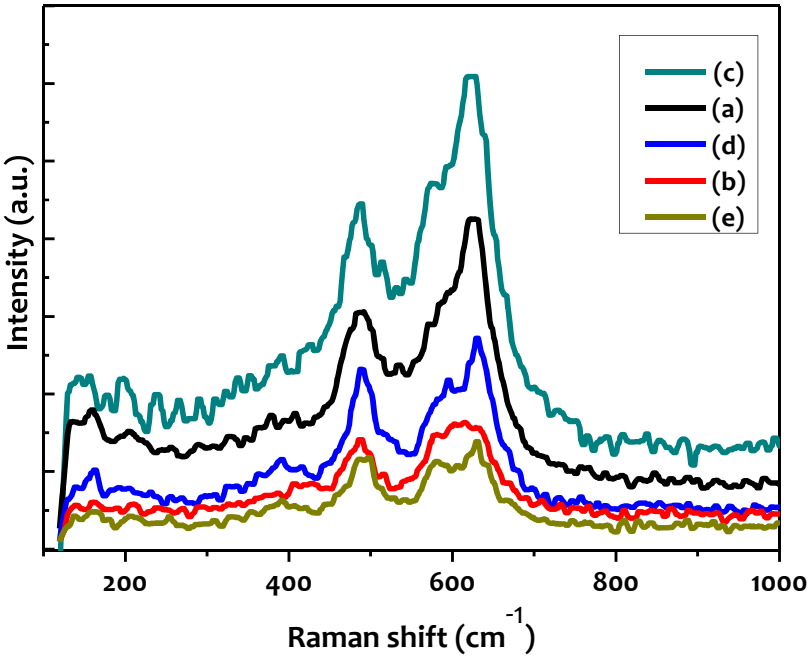

Figure 7.5: Raman spectra for (a) $LiMn_{1.5}Ni_{0.5}O_4$, (b) $LiMn_{1.48}Gd_{0.02}Ni_{0.5}O_4$, (c) $LiMn_{1.46}Gd_{0.04}Ni_{0.5}O_4$, (d) $LiMn_{1.46}Nd_{0.04}Ni_{0.5}O_4$, and (e) $LiMn_{1.46}Dy_{0.04}Ni_{0.5}O_4$ powders

7.2.4 Porosity and Specific Surface Area Study

The nitrogen adsorption-desorption isotherms and pore size distributions are exhibited in Figure 7.6 (a-b).

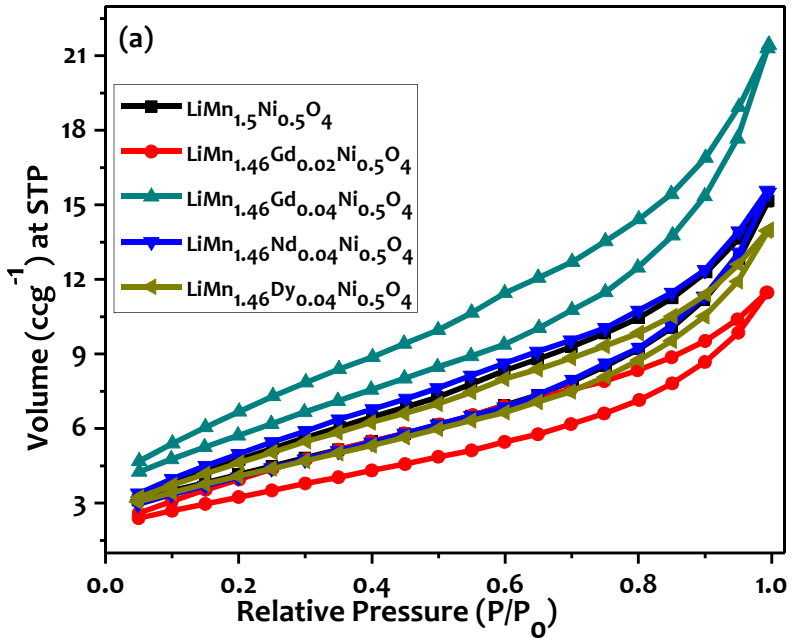

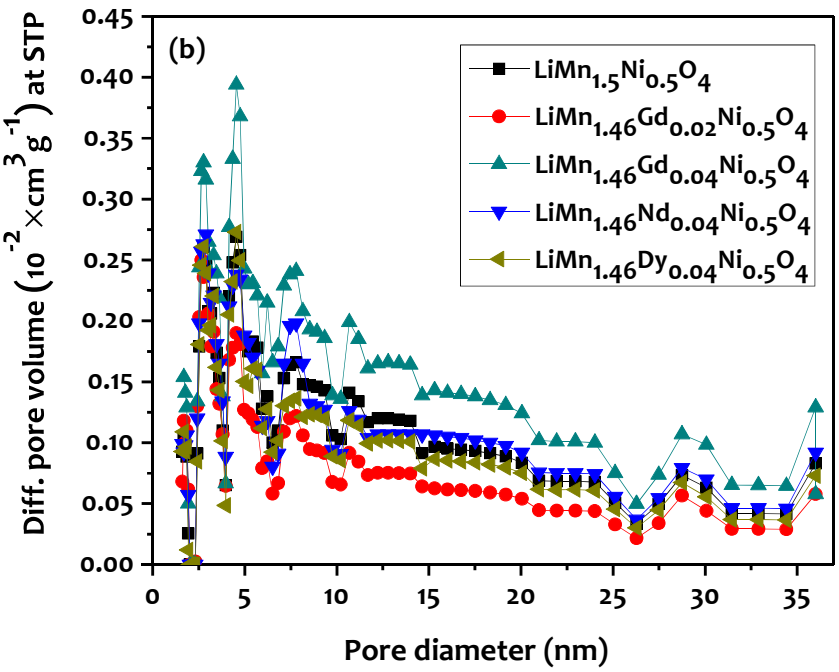

Figure 7.6: (a) Nitrogen adsorption - desorption isotherms and (b) Pore size distribution for $LiMn_{1.5}Ni_{0.5}O_4$, $LiMn_{1.48}Gd_{0.02}Ni_{0.5}O_4$ and $LiMn_{1.46}Ni_{0.5}RE_{0.04}O_4$ (RE: Gd, Nd, Dy) powders

The LMNO, LMNO-Nd04 and LMNO-Dy04 cathodes are exhibiting a meso-porous polyhedral crystal structure having 15 m^2/g specific surface area evaluated by multi point Brunauer-Emmett-Teller (BET) method and shown as in the Figure 7.6 (a). However, the specific surface area for LMNO-Gd04 material is calculated as 21 m^2/g whereas for LMNO-Gd02 material is determined as 12 m^2/g which is showing the increase in particle size with increasing Gd doping amount. The pore-size distribution, Figure 7.6 (b), reveals that the different materials show wide range of pore sizes from 2 to 35 nm, with an average pore size of 3 nm. Thus, synthesized cathode samples have a non-homogeneous and non-uniform surface morphology.

7.3 ELECTROCHEMICAL CHARACTERIZATION OF RARE-EARTH DOPED $LiMn_{1.5}Ni_{0.5}O_4$ CATHODES

The rare-earth element (Gd, Nd and Dy) doped cubic spinel phase LMNO cathode powders are characterized electrochemically to evaluate the influence of doped element. The electrochemical performances of active material are assessed by adopting cyclic voltammetry technique, galvanostatic charge-discharge technique, and AC impedance spectroscopy technique. These characterization techniques and their analysis are presented in subsequent sub-sections from 7.3.1 to 7.3.4 in phased manner as follows:

(7.3.1) *Cyclic voltammetry technique* is exploring the reduction and oxidation potentials.
(7.3.2) *Galvanostatic charge-discharge technique* is used to assess the specific charge-discharge capacities at different charging and discharging rate i.e. C-rate.
(7.3.3) *Rate performance and Cyclability measurements* are presenting the capacity fading, columbic efficiency at different C-rates. It also describes the charge-discharge cyclic behavior upto 50 cycles at Crate.
(7.3.4) *Electrochemical impedance spectroscopy* is assessing the total internal impedance of fabricated cathodes.

7.3.1 Cyclic Voltammetry and Its Analysis

To get more insight about the effect on redox potential of cathode materials, the cyclic voltammetric (CV) is carried out. The curves of cathodes, except for LMNO-Gd04 sample, are shown in Figure 7.7. The CV curve for LMNO-Gd04 cathode is not shown due to its higher impedance value (Figure 7.10). The redox potentials are measured and tabulated in Table 7.4. The first three successive cycles of CV curves are recorded for the LMNO-Gd02 cathode and shown in Figure 7.7 (a). It is revealed that the area under each peak is almost similar which supports the low electrochemical polarization effect in LMNO-Gd02. The Figure 7.7 (b) is presenting typical CV profiles with one weak pair of redox peaks at around 4.0 V which corresponds to Mn^{3+}/Mn^{4+}, as shown inset view in Figure 7.7 (b), and two pairs of well separated strong redox peaks at 4.6 - 4.7 V. These strong peaks are verifying two-stage (Ni^{2+}/Ni^{3+} and Ni^{3+}/Ni^{4+}) Li^{+}-ion extraction (insertion) from (into) the spinel framework. These redox potential peaks are also observed for each sample. The amount of current, Figure 7.7 (b), is decreasing for all doped samples in comparison with un-doped LMNO sample.

The two pair of redox peaks between 4.6 V and 4.7 V are appeared in all cathodes and summarized in Table 7.4. The symbols are defined as follows: E_{pa}: anodic peak potential, E_{pc}: cathodic peak potential. The numbers 1 and 2 denote the redox couple at lower and higher potential, respectively. Taking into account the results in table 7.4, it is observed that ΔE_{p1} and ΔE_{p2} are higher than the ideal condition ($\Delta E_p = 0$) which indicates that $Ni^{2+} \leftrightarrow Ni^{4+}$ is controlled by insertion/de-insertion of Li^{+}-ion in the cathode electrodes regardless of the sample.

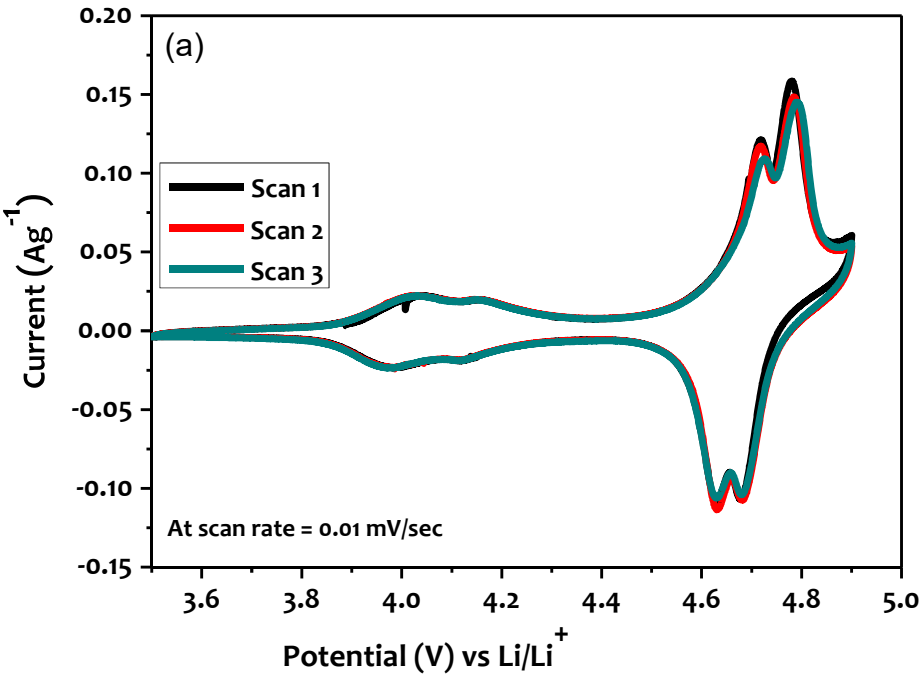

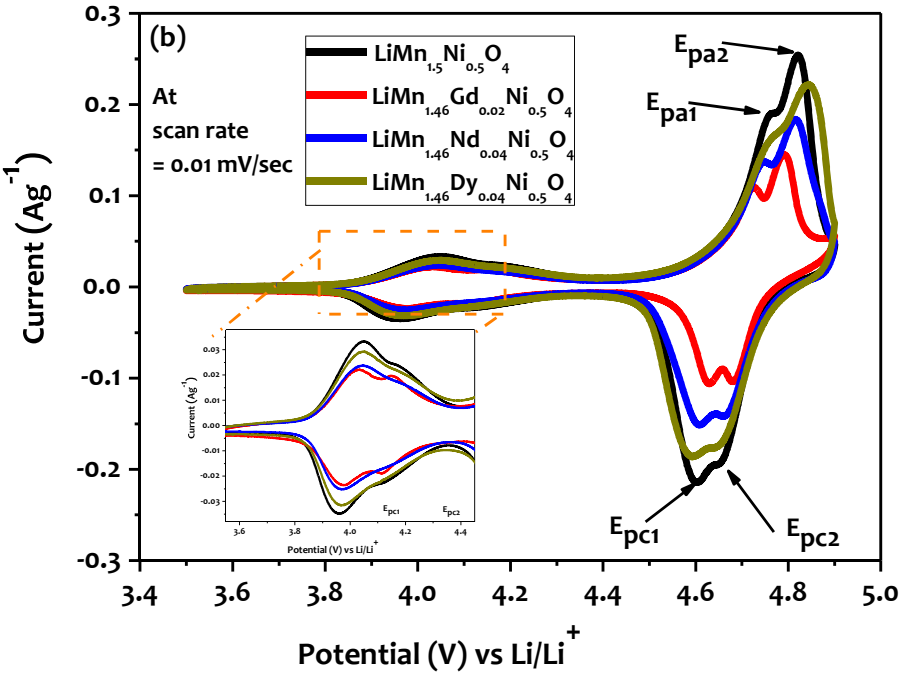

Figure 7.7: CV curves for (a) $LiMn_{1.48}Gd_{0.02}Ni_{0.5}O_4$ sample as a function of the scan number and (b) for $LiMn_{1.5}Ni_{0.5}O_4$, and $LiMn_{1.48}Gd_{0.02}Ni_{0.5}O_4$, $LiMn_{1.46}Nd_{0.04}Ni_{0.5}O_4$, and $LiMn_{1.46}Dy_{0.04}Ni_{0.5}O_4$ cathodes

Table 7.4: Redox Potentials for for$LiMn_{1.5}Ni_{0.5}O_4$, $LiMn_{1.48}Gd_{0.02}Ni_{0.5}O_4$ and $LiMn_{1.46}Ni_{0.5}RE_{0.04}O_4$ (RE: Gd, Nd, Dy) Cathodes

Sample Description	*Potential (V)*					
	E_{pa1}	E_{pa2}	E_{pc1}	E_{pc2}	ΔE_{p1}	ΔE_{p2}
LMNO	4.76	4.82	4.60	4.66	0.16	0.16
LMNO-Gd02	4.73	4.79	4.62	4.68	0.11	0.11
LMNO-Nd04	4.75	4.82	4.61	4.66	0.14	0.16
LMNO-Dy04	4.76	4.84	4.59	4.65	0.17	0.19

The lower values of ΔE_{p1} and ΔE_{p2} are due to the higher surface area value for the LMNO-Gd02 sample in comparison with the un-doped $LiMn_{1.5}Ni_{0.5}O_4$ sample. It indicates that lithium diffusion behavior is enhanced. As in Table 7.4, The potential difference follows the order $LiMn_{1.48}Ni_{0.5}Gd_{0.02}O_4$ <$LiMn_{1.46}Ni_{0.5}Nd_{0.04}O_4$ ≈ $LiMn_{1.5}Ni_{0.5}O_4$ <$LiMn_{1.46}Ni_{0.5}Dy_{0.04}O_4$, which indicating that the $LiMn_{1.48}Ni_{0.5}Gd_{0.02}O_4$ sample has lowest electrochemical polarization which is reflecting increased conductivity and lithium-ions diffusivity during extraction-insertion in the active material.

7.3.2 Galvanostatic Charge-Discharge Performance and Its Analysis

The charge-discharge study of fabricated 8 mm cathodes are performed on two electro Swagelok cell at different C-rates by adopting galvanostatic technique. At room temperature, the charge-discharge profiles after 5th cycle at different scan rates for LMNO and LMNO-Gd04 cathodes are shown in Figure 7.8 (a-b). The shape of the charge-discharge curves for the others RE doped LMNO powders are similar as presented in Figure 7.8 (c-d) with variations in the charge and discharge capacity.

Independent of the samples, Figure7.8 shows the three voltage plateaus are observed at ~ 4.0 V, 4.6 V and 4.7 V corresponding to Mn^{3+}-Mn^{4+}, Ni^{2+}-Ni^{3+} and Ni^{3+}-Ni^{4+} redox processes, respectively. These plateaus are also observed in cyclic voltammetry results [Figure 7.7(b)]. These plateaus are allocated to lithium-ion insertion into 16d octahedral and 8a tetrahedral sites

of spinel structure, respectively. From Figure 7.8 (a), the specific discharge capacities of LMNO cathode are recorded as 98.5, 101.7, 100.5, 89 and 32 mAh.g^{-1} at rates C/8, C/5, C/2, C and 2C, respectively. The low value of the discharge capacity at 2C is due to the formation of thicker solid electrolyte interface (SEI) layer and electrolyte decomposition at high voltage. Similarly, the specific discharge capacities for LMNO-Gd04 cathode, , are observed as 62.5, 70.6, 75.8, 74.5 and 65.9 mAh.g^{-1} at rates of C/8, C/5, C/2, C and 2C, respectively and Figure7.8(b).

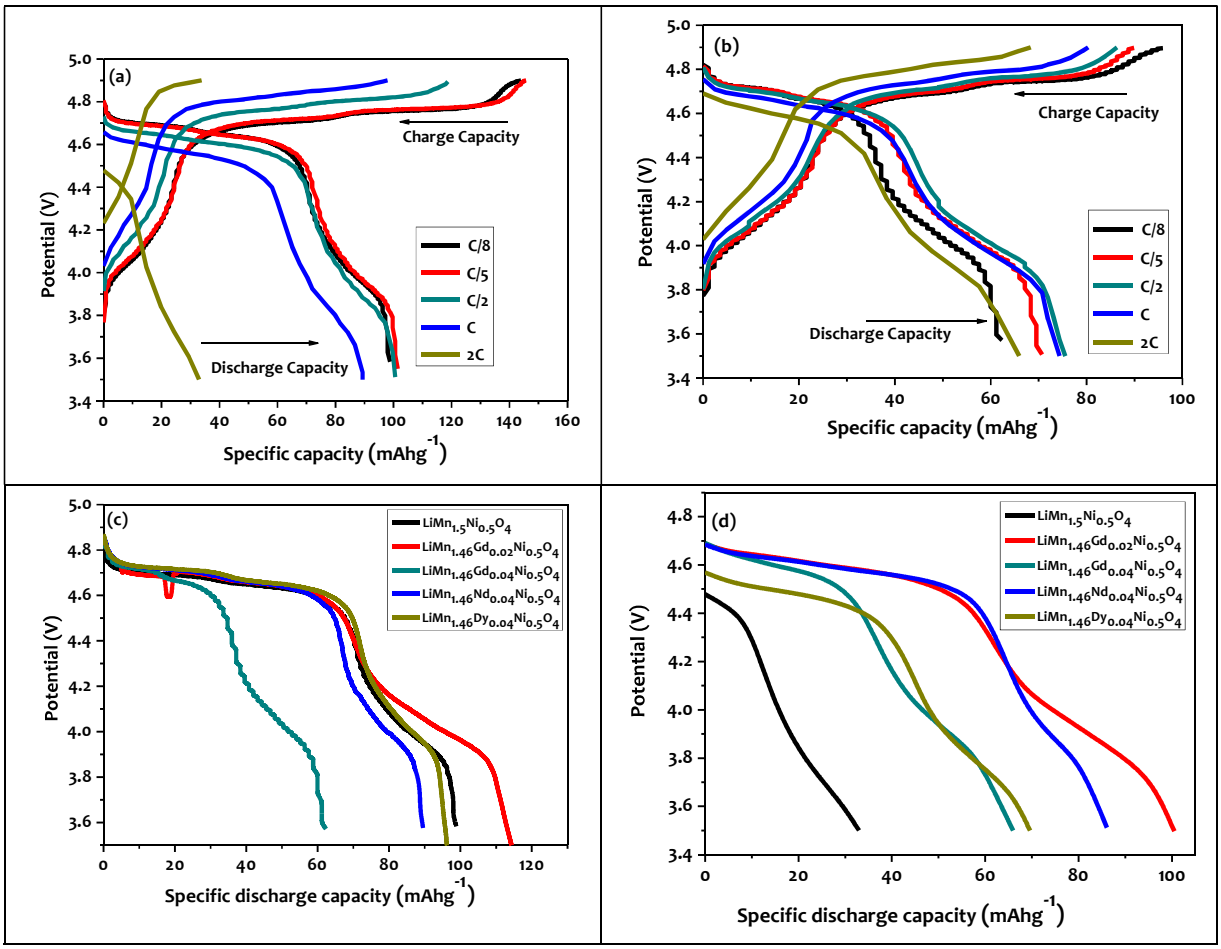

Figure 7.8: Charge–discharge curves at C/8 to 2C for the 5th cycle for: (a) $LiMn_{1.5}Ni_{0.5}O_4$ and (b) $LiMn_{1.46}Gd_{0.04}Ni_{0.5}O_4$ cathodes. Charge–discharge curves for all cathodes: (c) at C/8 and (d) 2C for the 5th cycle

The formation of the SEI layer and the irreversible capacity are observed higher for LMNO-Gd04 cathode compared with LMNO cathode due to its surface area value. It is conclusive that higher the surface area reduces the battery performance.

At room temperature, the discharge curves for all cathodes at C/8and 2C are shown in Figure 7.8 (c) and Figure 6.8 (d), atthe 5th cycle. It is shown that rare earth element doping affects the battery performance of LMNO cathode. The effect depends on doping element and amount. At 2C rate, the rare earth doped LMNO cathodes has more capacity compared to LMNO. The LMO-Nd04 has more flat plateau at 4.6 V which indicated that at higher specific discharge capacity of LMNO-Nd04 at high C-rate.

The specific discharge capacity of cathodes is observed as at C/8 (LMNO: 99.3 mAhg^{-1}; LMNO-Gd02: 113.7 mAhg^{-1}; LMNO-Gd04: 62.5 mAhg^{-1}; LMNO-Nd04: 89.5 mAhg^{-1}; LMNO-Dy04: 96.9 mAhg^{-1}) and at 2C (LMNO: 32.8 mAhg^{-1}; LMNO-Gd02: 100.3 mAhg^{-1}; LMNO-Gd04: 65.9 mAhg^{-1}; LMNO-Nd04: 86.2 mAhg^{-1}; LMNO-Dy04: 69.2 mAhg^{-1}). The decrement at 2C is due to electrochemical SEI layer effect. It is also observed for the scan rate of 2C, the 4.7 V discharge voltage plateau decreases and the 4.0 V plateau slowly disappears as in Figure 7.8(d).

The RE doped LMNO-Gd02, LMNO-Nd04 and LMNO-Dy04 cathodes are demonstrating a higher specific discharge capacity in comparison with the pristine LMNO. It is evident that rare earth element doping affects the discharge capacity value of the LMNO cathode material. The intermediate surface area of LMNO-Gd02, LMNO-Nd04 and LMNO-Dy04 cathodes are enhancing the electrochemical efficiency through the intercalation and de-intercalation processes of the Li^+ ions.

7.3.3 Rate Performance and Cyclability Analysis

The discharge rate performances of the different rare earth doped cathodes at different C-rates are demonstrated in Figure 7.9 (a). Rate capability of theses cathode materials is influenced by several factors as lithium-ion diffusion through the SEI layer, charge transfer resistance and ohmic polarization. All the cathode samples, Figure7.9 (a), show very stable discharge capacity value for each scan rate as a function of the cycle number, particularly for scan-rates above C/2. The columbic efficiency (CE), related to the reversibility of the process, is approximately 90% for all the cathode materials doped with rare earth element.

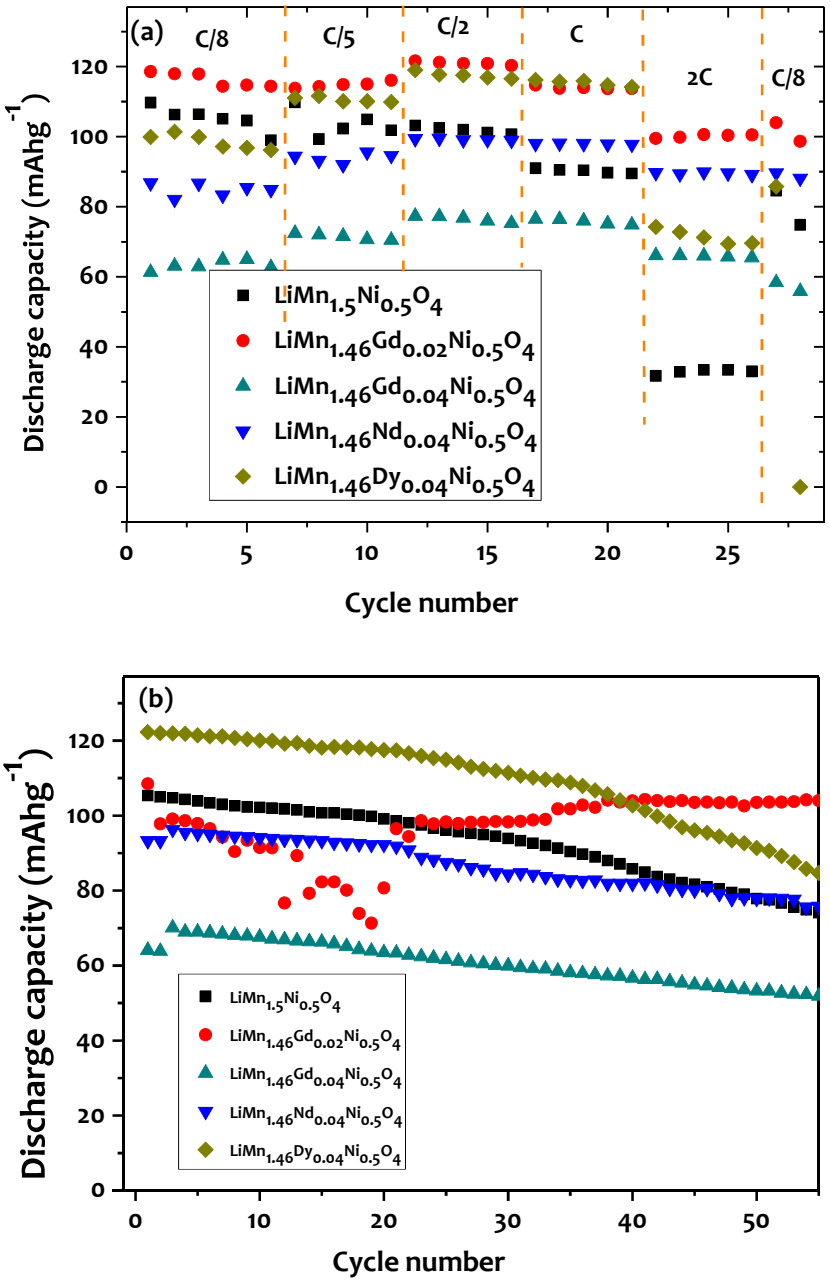

Figure 7.9: (a) Rate performance and (b) Cycling performance for the different cathodes

The cathode material LMNO-Gd02 is offering improved rate performance in comparison with other cathodes. Also, LMNO-Nd04 and LMNO-Dy04 cathodes show higher discharge capacity value compared to un-doped LMNO cathode for above 1C scan-rates. Moreover, when the recovery cycle is performed at C/8 rate after cycling at various C-rates, the discharge capacity of all the samples is achieved more than 90% of initial values. It is indicating good reversibility of cathode materials. Further, rare-earth doping tends to stabilize the crystal structure and suppress Mn^{3+} dissolution as is the case for LMNO-Nd04 and LMNO-Dy04 samples. The low amount of doping, LMNO-Gd02, is supporting in stable cycling. The improved rate performance of rare earth element doping is being attributed to the high surface area value and stabilization of the structure.

At room temperature, the Cyclability of doped cathode at C-rate is presented in Figure 7.9 (b). It is observed that rare earth element and amount doping has potential to improve the cyclic performance of LMNO cathode. After 50 cycles, the discharge capacity is measured as 105 $mAhg^{-1}$, 84.6 $mAhg^{-1}$, 75.7 $mAhg^{-1}$, 73.8 $mAhg^{-1}$ and 51.9 $mAhg^{-1}$ for LMNO-Gd02, LMNO-Dy04, LMNO-Nd04, LMNO, and LMNO-Gd04, respectively. It is demonstrating that LMNO-Gd02 shows the best cyclability and structural stability. Morever, neodymium (Nd) and Dysprosium (Dy) are also improving the cycling stability of LMNO spinel cathode.

For the initial twenty cycles, the specific discharge capacity is fluctuating for LMNO-Gd02 cathode which may be related to the daily fluctuation of the ambient temperature affecting battery temperature. However, the exact reason for this is not clear and need for further investigation. The poor cycling performance of LMNO-Gd04 cathode can be presumably attributed to the surface reactivity of the sample in contact with the liquid electrolyte.The table 7.5 shows different parameters calculated from the results in Figure 7.9 (b) at C-rate based on the charge-discharge curves for the different cathodes.

Table 7.5: Charge and Discharge Capacities for RE doped LMNO Cathodes at C at Room Temperature

Sample Description	Initial Charge Capacity (±3) $mAhg^{-1}$	Initial Discharge Capacity (±3) $mAhg^{-1}$	2nd Discharge Capacity (±3) $mAhg^{-1}$	55th Discharge Capacity (±3) $mAhg^{-1}$	Initial Capacity Loss (%)	55th Cycle Capacity Loss after (%)
LMNO	115.1	105.3	105	74.1	8.5	29.6
LMNO-Gd02	139.6	108.5	97.8	104.0	22.2	4.15
LMNO-Gd04	90.5	64.1	63.8	51.9	29.2	19.0
LMNO-Nd04	108.1	93.3	93.3	75.8	13.7	19.0
LMNO-Dy04	128.4	122.3	122.0	84.7	4.8	30.7

The initial specific charge and discharge capacities (Table 7.5) are pointed out the enhanced capacity for the doped LMNO cathode electrodes due to the addition of Gd^{3+} and Dy^{3+} in the LMNO-Gd02 and LMNO-Dy04 cathode materials that are affected by the surface area value. After 55 cycles, capacity fades 4.15% for LMNO-Gd02 and 19% for LMNO-Nd04 and LMNO-Gd04, in comparison to the value of 29.6% observed for LMNO cathode.

7.3.4 Electrochemical Impedance Spectroscopy

The Electrochemical impedance spectroscopy (EIS) measurements were carried out to understand further the effect on electrical conductivity and total internal impedance of rare earth doped cathodes. As in Figure 7.10 (a-b) showed that rare-earth doping improves rate performance and cycling life. The impedance spectra before cycling and after 55^{th} cycles are shown in Figure 7.10 (a & b).

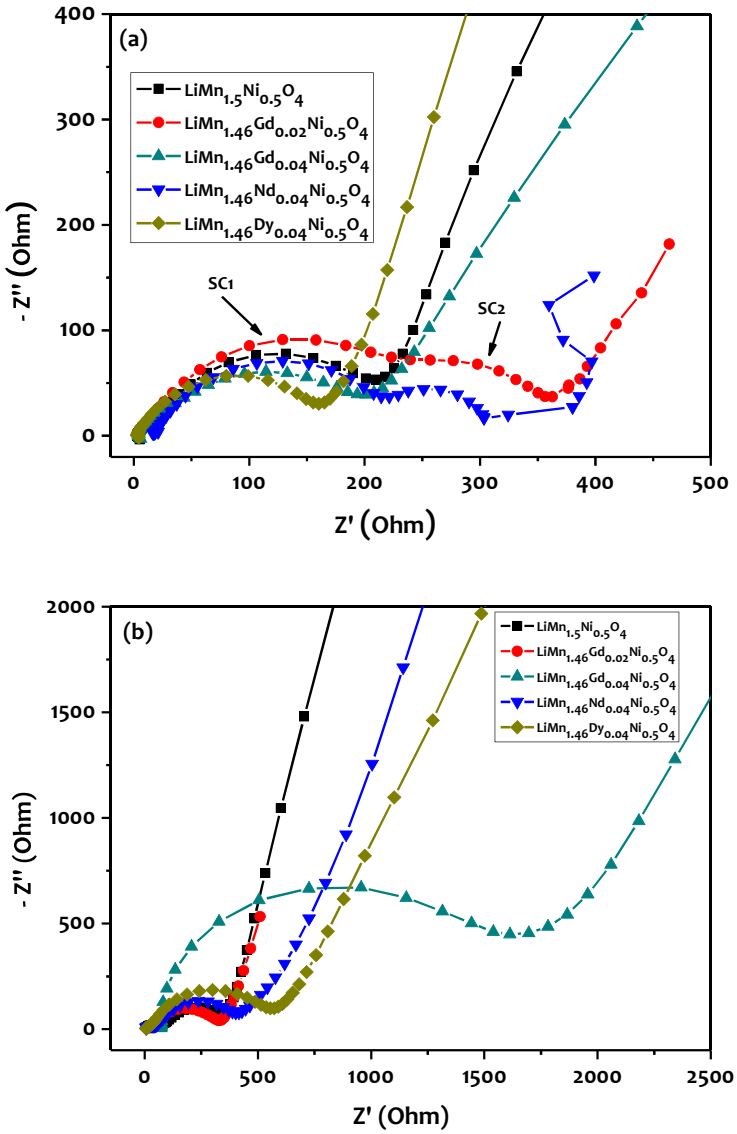

Figure 7.10: EIS spectra of RE doped LMNO cathodes (a) before and (b) after cycling

The impedance spectra of all cathode samples before cycling, Figure 7.10 (a), are characterized by two semicircles in high-to-medium frequency region followed by a straight line in the low-frequency region. These two semi-circles are described by the contributions of three resistances: the ohmic resistance (liquid electrolyte resistance) given by the intercept of the Z_{re} axis at high frequency; the first semicircle which is ascribed to surface resistance (R_s, solid-electrolyte interface (SEI) layer); and the second semicircle which is assigned to the charge-transfer resistance process (R_{ct}) .The slope in the low-frequency region represents the Warburg impedance, which is associated with Li^+-ion diffusion in the bulk material. These semicircles (SC1 and SC2) are identified in the Figure 7.10 (a) through an arrow.

The shape of impedance curves after cycling as shown in Figure 7.10 (b), are similar to those before cycling as shown in Figure 7.10 (a), which reveal that the rare-earth doping does not affect its shape. The cumulative impedance value is the summation of aforementioned resistances. The values of these resistances before and after cycling for the different cathodes are enlisted in Table 7.6.

Table 7.6: Total Impedance Obtained Before Cycling and After 55th Cycle for All Cathodes

Samples Description	Before cycling (Ω)	After cycling (Ω)
LMNO	210	343
LMNO-Gd02	362	337
LMNO-Gd04	203	1685
LMNO-Nd04	340	413
LMNO-Dy04	160	566

It is observed that before cycling the lowest resistance value, 160 is obtained for the LMNO-Dy04 material whereas other cathodes have resistance value in range 202 -362 Ω. After cycling, the total resistance value increases for all samples in comparison with its value before cycling except for the LMNO-Gd02 cathode. This incremente in resistance is due to the SEI formation. This interesting feature is observed for the $LiMn_{1.48}Ni_{0.5}Gd_{0.02}O_4$ cathode. The resistance before cycling and after cycling is as 362 Ω and 337 Ω which show reduction that is in contrast to other cathode samples. It is evident from Figure 7.10 and Table 7.6 that LMNO-Gd02 cathode presents low resistance value after cycling in comparison to the value before cycling which is indicating that this doping suppresses the growth of SEI, which is likely related to the improvement of the cycling stability [Figure 7.9 (b)]. The main reason for this fact is the low surface area of this sample and also that small Gd doping reduces Mn dissolution, which results in more stable SEI layer after cycling.

7.3.5 Comparison of Current Work with Previous Work

It is very useful to compare the electrochemical performance of the current samples with other doping reported in the literature for $LiMn_{1.5}Ni_{0.5}O_4$ based cathodes once. This is the first of study about different rare earth elements doped in the spinel LMNO cathode structure. Though, powder size and composition of cathode electrode, which are reported in table 7.2, are not same for all samples. It is observed that the samples presented in this work are best among the best reported in the literature as tabulated in Table 7.7, the rare earth doping improving the cyclability of the LMNO spinel cathode at room temperature.

Due to their unusual physical and chemical properties and also to the fact that the rare earth elements presented in this work are more abundant on average in the Earth's crust than silver, gold, or platinum [USGS, 2017]. By taking into account the abundance, the rare earth metals doping in LMNO cathode is an excellent alternative for conventional doping to solve the problem of capacity fade as it is shown in table 7.7.

Table 7.7: Comparison of the Discharge Capacity for RE and other Element Doped $LiMn_{1.5}Ni_{0.5}O_4$ Reported in the Literature

Cathode Description	Element doping	Particle Size (μm)	Discharge Capacity (mAhg-1)	Reference
$LiMn_{1.4}Cr_{0.2}Ni_{0.4}O_4$	Cr	< 1	130.8 at 0.15C	Yi T-F. et al 2009
$LiNi_{0.5}Mn_{1.5}O_{3.975}F_{0.05}$	F	-----	142 at 0.25C	Xu, X.X., et al 2007
$LiMn_{1.5}Ni_{0.42}Fe_{0.08}O_4$	Fe	~ 1	136 at C/6	Liu,J. and Manthiram A., 2009
$LiMn_{1.5}Ni_{0.42}Ga_{0.08}O_4$	Ga		~ 128 at C/6	Shin,D.W., et al. 2011
$LiMn_{1.4}Ni_{0.55}Mo_{0.05}O_4$	Mo	3-5	122.7 at 0.1C	Yi. T-F, et al., 2014
$LiNi_{0.525}Mn_{1.425}Nb_{0.05}O_4$	Nb	1-2	102.7 at C	Yi. T-F, et al., 2012
$LiNi_{0.48}Rh_{0.02}Mn_{1.5}O_4$	Rh	0.08	92.4 at C	Wu.p. et al, 2013

$LiNi_{0.5}Mn_{1.5}O_{3.95}S_{0.05}$	S	0.01	116 at 0.2C	Sun Y.K., 2006
$LiNi_{0.5}Mn_{1.0}Ti_{0.5}O_4$	Ti	< 1	206.5	Lin,M., et al, 2013
$LiNi_{0.4}Ti_{0.1}Mn_{1.5}O_4$	Ti	0.3 - 3.0	134.8 at C	Jin,Y.Z., et al., 2014
$Li_{0.995}V_{0.005}Ni_{0.5}Mn_{1.5}O_4$	V	0.1 - 0.2	130 at 0.8C	Kim, M.C., et al 2014
$LiW_{0.005}Ni_{0.5}Mn_{1.495}O_4$	W	0.5	124.9 at 0.1C	Prabakar, SJR, et al, 2012
$LiZn_{0.08}Ni_{0.42}Mn_{1.5}O_4$	Zn	-----	118 at 0.5C	Yang Z et al., 2014
$LiMn_{1.48}Ni_{0.5}Gd_{0.02}O_4$	Gd	0.05-0.2	104 at C	This work

7.4 CLOSING REMARKS

The rare-earth element, RE: Gd (0.02, 0.04), Nd (0.04) and Dy (0.04), doped LMNO cathodes are synthesized by organic sol–gel method. The rare earth doping does not affect the formation of a cubic spinel structure. The rare earth doping with Gd and Dy exhibits better electrochemical cycling performance in comparison to pristine $LiMn_{1.5}Ni_{0.5}O_4$. After 55 cycles at C, the discharge capacity values are recorded as 104 $mAhg^{-1}$, 84.7 $mAhg^{-1}$ and 74.1 $mAhg^{-1}$ for $LiMn_{1.48}Ni_{0.5}Gd_{0.02}O_4$, $LiMn_{1.46}Ni_{0.5}Dy_{0.04}O_4$, and $LiMn_{1.5}Ni_{0.5}O_4$, respectively. Further, the reduction in internal impedance is observed in Gd and Dy doped cathodes which suggest that electrical conductivity of these cathode electrodes is enhanced.

In summary, $LiMn_{1.48}Ni_{0.5}Gd_{0.02}O_4$ is an excellent active material for cathodes in rechargeable lithium-on battery applications at C-rate.